

Supplementary Materials: Probing the Deuteron at Very Large Internal Momenta

Event Selection Cuts

Figures 1–5 show the event selection cuts for data (blue hatched) and SIMC (red data points) for the deuteron 80 MeV/c kinematic setting at $\theta_{nq} = 35 \pm 5^\circ$. The black dashed or red solid lines (for collimators) represent the cuts or geometrical (collimators) boundaries used to select true ${}^2\text{H}(e, e'p)n$ coincidence events. The exact same cuts were also applied to the 580 and 750 MeV/c settings. Each histogram has all the other event selection cuts described except a self cut. The integrated counts (within the cut boundary) for data and simulation as well as the data-to-simulation yield ratio is shown (top left) for each selection cut. The data yield has been normalized by the total charge and corrected for the inefficiencies described in the Letter. The FSI model from J.M. Laget was used in the simulation for the plots shown below.

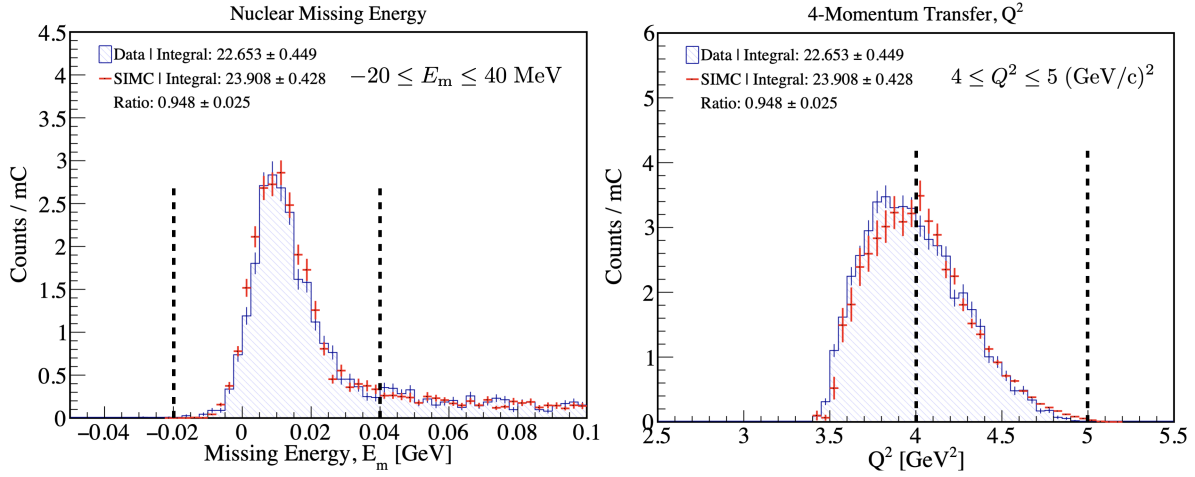


FIG. 1. Event selection cuts on missing energy (left) and 4-momentum transfer (right).

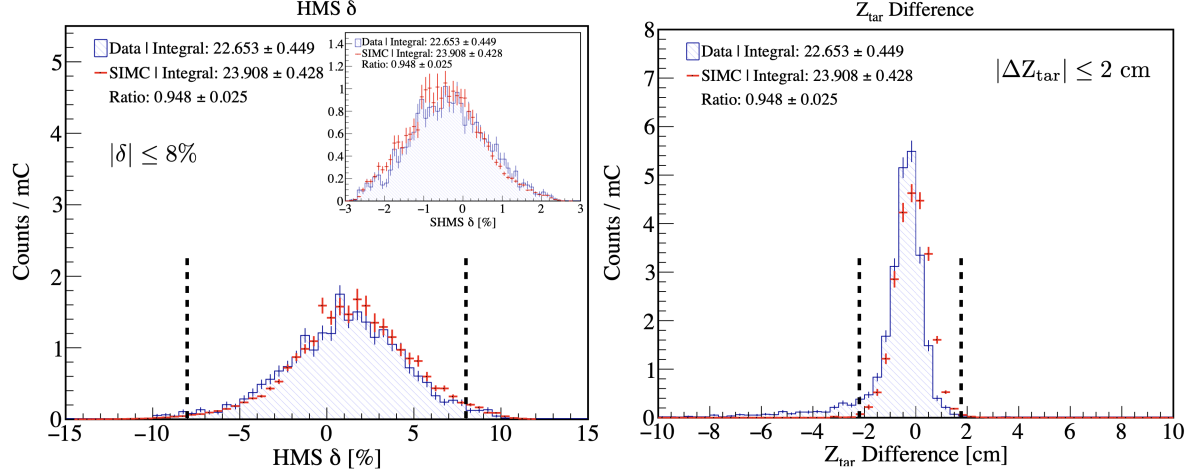


FIG. 2. Acceptance cut on HMS momentum fraction (left) and event selection cut on the difference between the z -reaction vertex on both spectrometers (right). Inset (left): The SHMS momentum acceptance range.

Figure 1 (left) shows the primary cut used to select true ${}^2\text{H}(e, e'p)n$ coincidence events by requiring a missing energy cut around the deuteron binding energy (~ 2.2 MeV) using the missing energy formula, $E_m = \omega - T_p - T_r$, where T_p is the final proton kinetic energy and T_r is the recoil particle kinetic energy which is calculated from the electron and proton 4-momentum vectors assuming an exclusive three-body final state with a recoiling neutron. The peak is not exactly at the deuteron binding energy because energy loss corrections have not been applied to the data nor SIMC.

Figure 1 (right) shows a kinematical cut made on the 4-momentum transfer at $Q^2 = 4.5 \pm 0.5$ (GeV/c)² to select events only at the highest possible momentum transfers to further suppress MEC and IC.

Figure 2 (left) shows a momentum acceptance (δ) cut made on the HMS in the range $8\% \leq \delta \leq 8\%$, where the optics reconstruction is reliable and well understood from previous experiments in the 6 GeV era. The inset shows the SHMS momentum acceptance which was constrained by that of the HMS to be $|\delta| \lesssim 3\%$ which is well within the reliable SHMS momentum acceptance range of $-10 \leq \delta \leq 22\%$. Figure 2 (right) shows reaction vertex cut on the difference between the HMS and SHMS reconstructed reaction vertices along the z -coordinate (target length). The cut is made at ± 2 cm relative to the histogram peak. If the events originated from the same reaction vertex (i.e., true coincidences), the difference should peak at zero with a finite resolution width. If the events are uncorrelated (i.e., accidental coincidences), however, the reconstruction along the z_v -vertex can vary significantly between the two spectrometers, which contribute to the tails of the distribution.

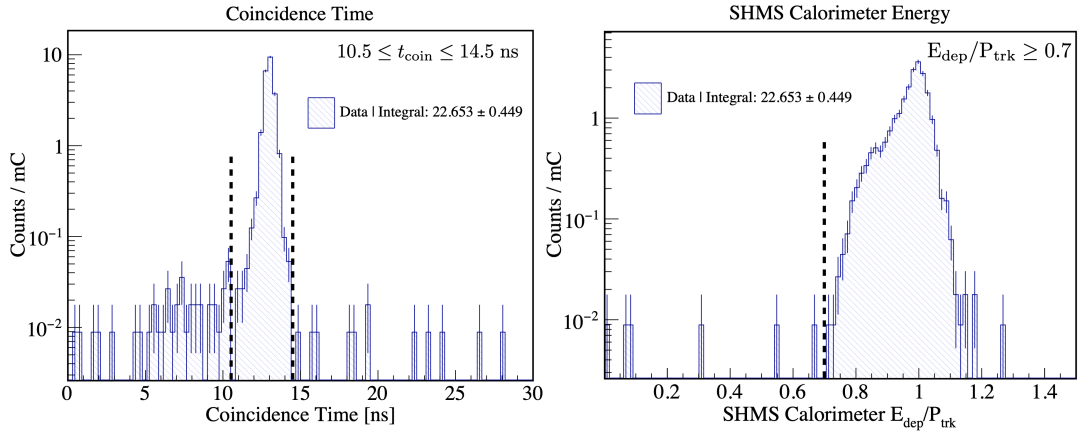


FIG. 3. Event selection cuts on the electron-proton (ep) coincidence time (left) and total deposited energy on calorimetered normalized by the particle track momentum (right).

Figure 3 (left) shows a coincidence time cut on the ep coincidence time spectrum formed by requiring a logic signal of at least 3 out of 4 scintillator planes between both spectrometers. The spectrum is very clean as the typical 2 ns beam bunch structure due to accidental coincidences is not observed. The out-of-time events observed at the tails can originate from the radiation in the Hall partially entering the detector huts and forming a trigger in coincidence with the other arm. Figure 3 (right) shows a particle identification cut on the SHMS calorimeter total energy deposited normalized by the particle track momentum. This cut was used to separate electrons from background (pions), however, the spectrum shows a very clean distribution with a peak at about one indicating the detected particles were electrons.

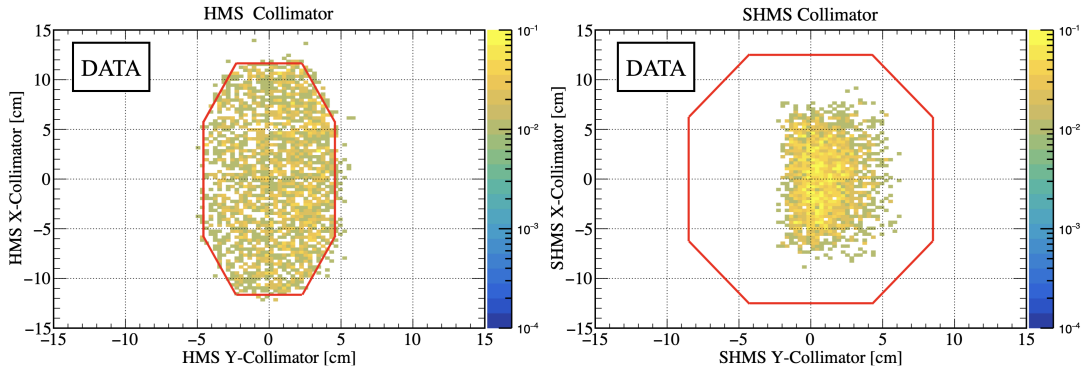


FIG. 4. (left) Geometrical acceptance cut on reconstructed events projected at the HMS collimator. (right) The SHMS events (correlated with HMS events on left plot), projected at the SHMS collimator.

Figure 4 (left) shows a geometrical (red octagon) cut on the reconstructed events projected at the HMS collimator to ensure that all events that enter the spectrometer pass through the collimator, and not re-scatter at the edges. This cut is needed since protons that enter the HMS can punch through the collimator with a probability that is related to the proton-Tungsten total cross section. Figure 4 (right) shows the correlated events projected at the SHMS collimator which clearly shows that the events are well within the collimator which indicates that the SHMS acceptance is driven by that of the HMS. Figure 5 shows the same acceptance cuts as previously described, but for simulation. The colored z -axis in both figures is given in arbitrary units.

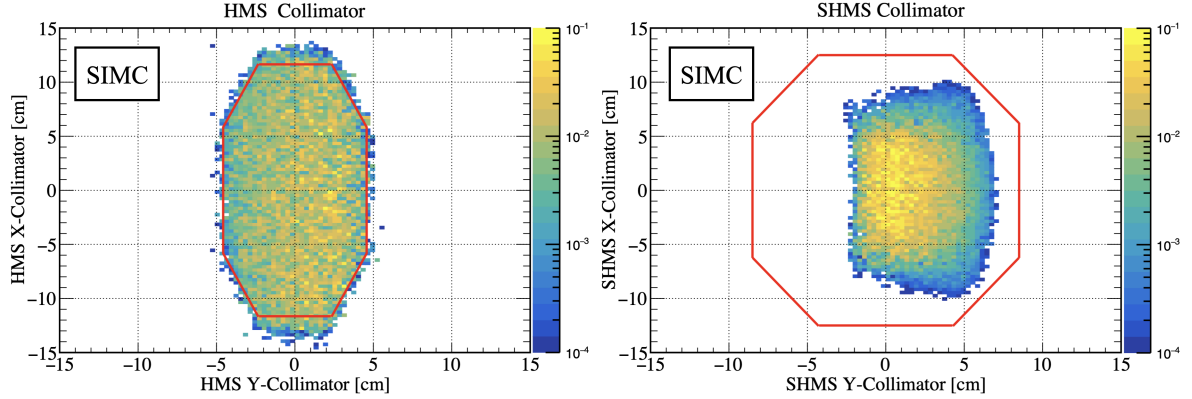


FIG. 5. Same as Fig. 4, but for simulation.

Deuteron Kinematic Distributions

Figures 6 and 7 show the fundamental kinematic variable distributions for each of the central missing momentum settings at $\theta_{nq} = 35^\circ$ and 45° . The data has been normalized by the total charge and corrected for the inefficiencies described in the Letter. The same event selection cuts mentioned in the previous section were applied.

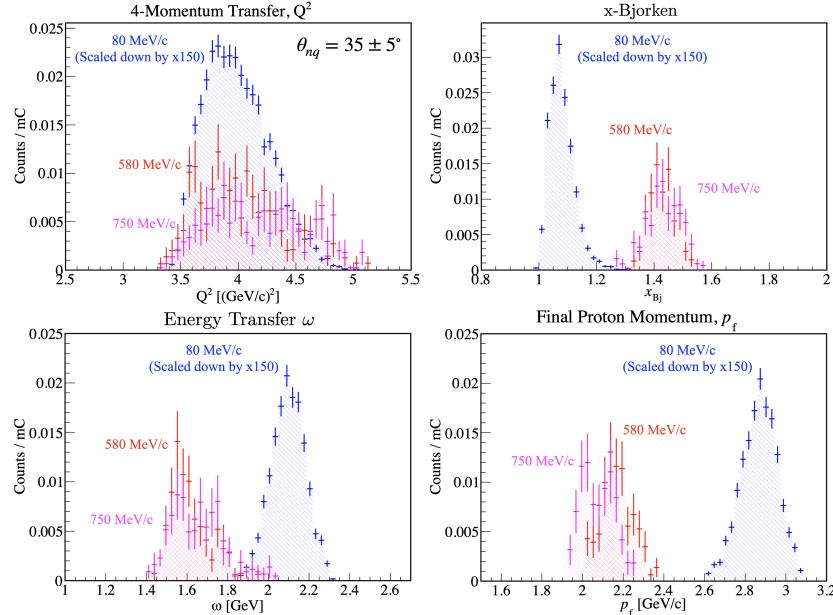
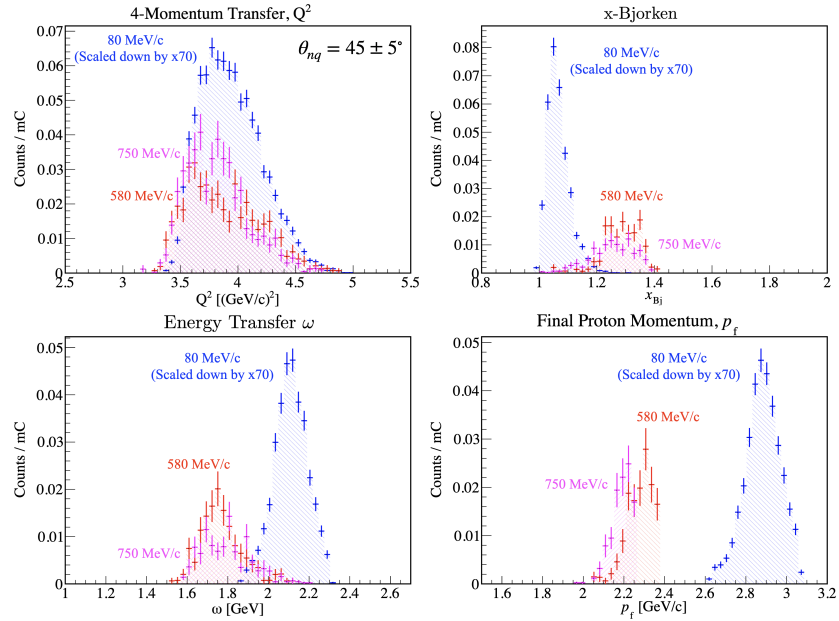


FIG. 6. Deuteron kinematic distributions for the 80 (blue), 580 (red) and 750 (magenta) MeV/c setting at $\theta_{nq} = 35^\circ$.

FIG. 7. Same as Fig. 6, but for $\theta_{nq} = 45^\circ$

Estimate of the Target Cell Endcaps Contribution to the Data Yield

To estimate the contribution to the yield due to the electron interaction with the aluminum endcaps of the target cell, a sample of events were selected in the negative part of the missing energy spectrum using the deuteron high missing momentum settings (580 and 750 MeV/c). We assume that the contribution due to the target endcaps is constant across the missing energy spectrum, therefore, by selecting a sample in the negative part of the spectrum over a specific range, we can estimate the endcaps contribution beneath the deuteron missing energy peak over the same range.

Figure 8 shows the missing energy spectrum for the 580 MeV/c setting (left) and the corresponding reconstructed SHMS z -vertex (right) for the specified range. The integral over endcaps and ${}^2\text{H}(e, e'p)n$ events show that the contribution from the cell walls has an upper limit of $0.00806/0.275 \sim 0.0293$ or approximately 2.9 % as the integral was done over all recoil angles, θ_{nq} . This result was added quadratically to the overall normalization error.

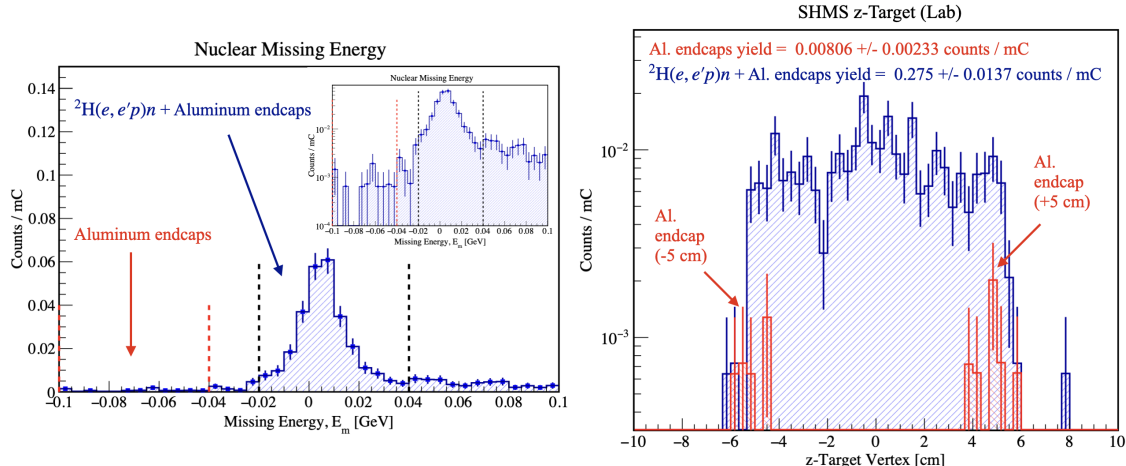


FIG. 8. (left) Missing energy spectrum for the deuteron 580 MeV/c setting with event selection region corresponding to Aluminum endcaps (in red) and deuteron missing energy peak over a 40 MeV range, each. (right) The SHMS z -reaction vertex corresponding to the specified region in the missing energy spectrum. Inset (left): Missing energy spectrum on a logarithmic scale.

Cross-Section Extraction

The average experimental cross section was extracted by taking the ratio of the radiative corrected data yield (Y_{corr}) to the Monte Carlo generated phase space volume for each kinematic bin in (θ_{nq}, p_r) . For illustration purposes, Fig. 9 shows the experimental data yield (left) and the spectrometers' phase space volume (right) binned in missing momentum and integrated over all θ_{nq} bins for each of the three central momentum settings. A detailed discussion of how the experimental and reduced cross sections were extracted can be found in Sections 5.1 and 6.1 of Ref. [3].

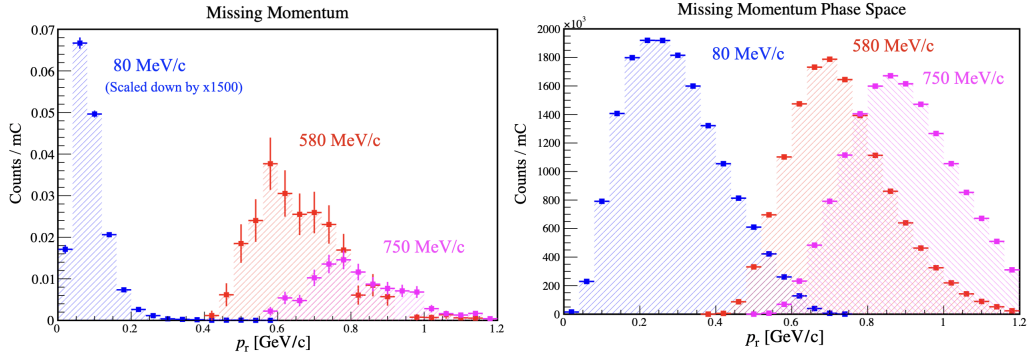


FIG. 9. (left) Experimental neutron recoil (“missing”) momentum distribution for each of the three central settings. (right) Monte Carlo (un-weighted) events generated over the spectrometers’ phase space volume binned in missing momentum.

Radiative & Bin-Centering Corrections

The radiative corrections were applied by multiplying the ratio of non-radiative to radiative SIMC yields to the data yield for each (θ_{nq}, p_r) kinematic bin as described in the Letter. The radiative correction factors for $\theta_{nq} = 35^\circ$ and 45° are shown in Fig. 10. The calculation was done using the Laget PWIA and FSI models for systematic effect studies, but the FSI model was ultimately used to correct the data yield. The uncertainty in the radiative correction factor was determined by the Monte-Carlo statistics from the simulation. The large uncertainty in the lowest momentum bin, $p_r = 0.02 \pm 0.02$, can be understood from the fact that statistics were limited in this phase space region as indicated by the “hole” observed at $p_r = 0.02$ in Fig. 9 (right).

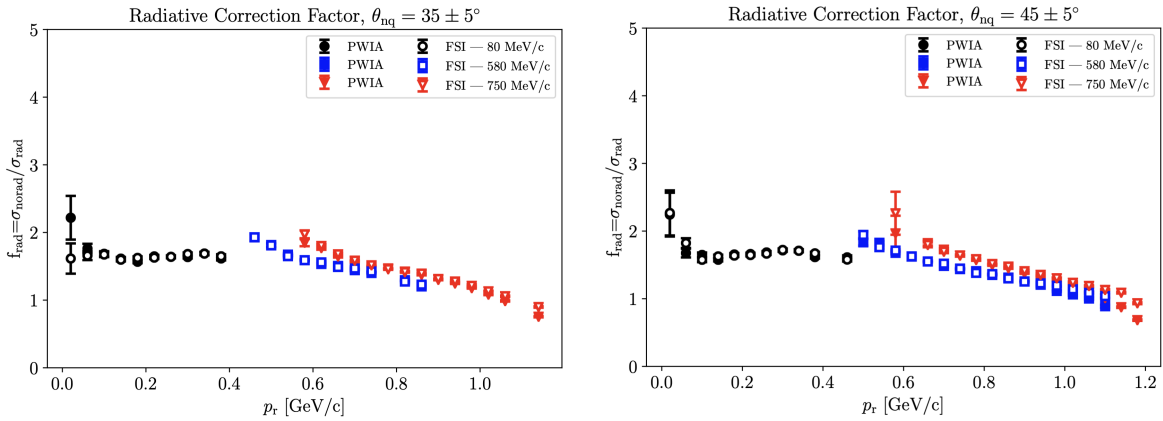


FIG. 10. Radiative correction factor versus neutron recoil momenta, p_r , for $\theta_{nq} = 35^\circ$ (left) and 45° (right).

The bin centering corrections were applied by multiplying the ratio, $f_{bc} \equiv \sigma_{\text{avg.kin}}/\bar{\sigma}$, to the average data cross section over each (θ_{nq}, p_r) kinematic bin, as described in the Letter. The bin centering correction factors for $\theta_{nq} = 35^\circ$ and 45° are shown in Fig. 11. The calculation was done using the Laget PWIA and FSI models for systematic effect studies, but the FSI model was ultimately used to correct the data cross section. The uncertainty in the bin-centering correction factor was determined from the standard error propagation of a ratio between two quantities.

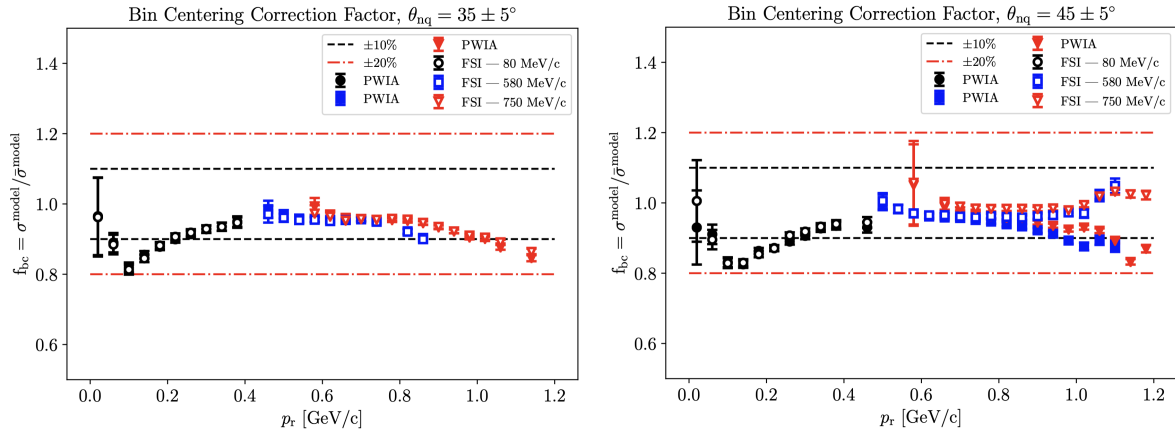


FIG. 11. Bin centering correction factor versus neutron recoil momenta, p_r , for $\theta_{nq} = 35^\circ$ (left) and 45° (right). The inner (black dashed) and outer (red dash-dotted) lines represent a percent deviation from unity of $\pm 10\%$ and $\pm 20\%$, respectively.

Systematic Uncertainty Studies on Radiative and Bin-Centering Corrections

The systematic effect on the cross sections due to model dependency of the radiative and bin-centering corrections was investigated (see Section 5.10 of Ref.[3]) using the Barlow ratio approach [1, 2]. In this case, the ratio was calculated from the difference between the experimental cross sections using the Laget PWIA and FSI models for both radiative and bin-centering corrections. Figures 12 and 13 show the Barlow ratio for radiative and bin-centering systematics is mostly within 2 standard deviations which show that the model dependency of the correction factors have a negligible effect on the experimental cross sections.

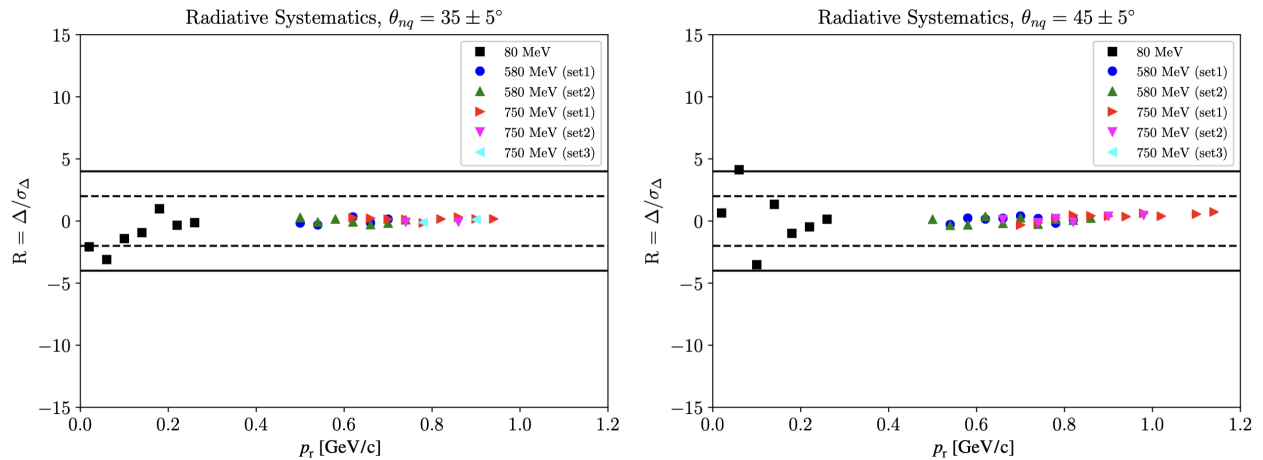


FIG. 12. Systematic effects of the radiative corrections model dependency on the data cross sections for $\theta_{nq} = 35^\circ$ (left) and 45° (right). The inner (black dashed) and outer (black solid) lines represent the $\Delta = \pm 2\sigma_\Delta$ and $\pm 4\sigma_\Delta$ boundaries, respectively.

Systematic studies of the event selection cuts described above were also carried out using the R. Barlow approach. The studies demonstrated that variations in the software had a negligible effect in the measured cross sections and thus no systematic uncertainties due to software cuts were included in the final result. For a detailed discussion of these studies see Section 5.10 of Ref.[3].

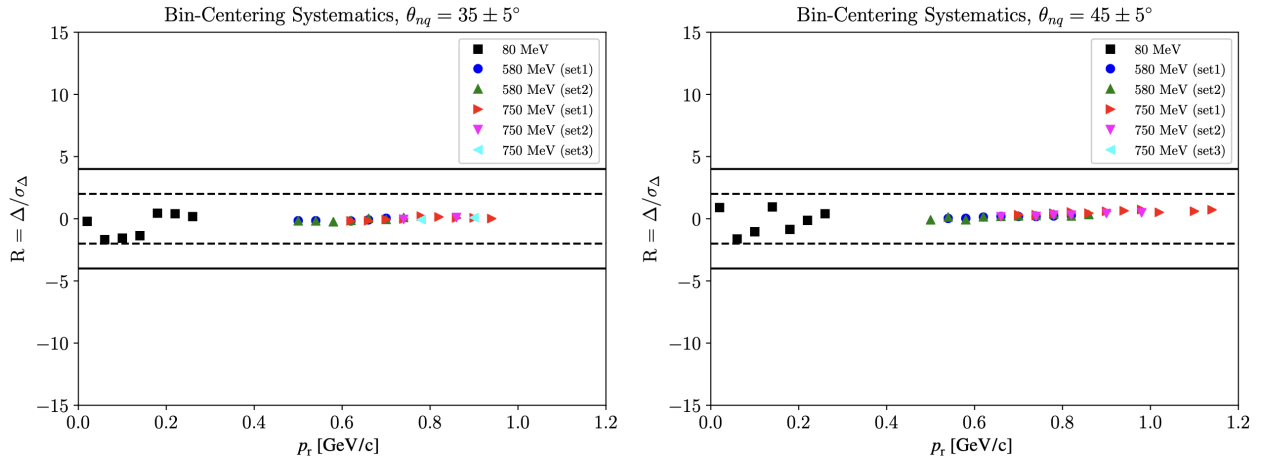


FIG. 13. Same as Fig. 12 but for bin-centering correction systematics.

-
- [1] R. Barlow, Systematic Errors: facts and fictions (2002), <https://arxiv.org/abs/hep-ex/0207026> [hep-ex].
 - [2] R. Barlow, Systematic Errors in Particle Physics (2017), https://indico.cern.ch/event/591374/contributions/2511753/attachments/1429002/2193943/01_PWA-Barlow.pdf.
 - [3] C. Yero, *Cross Section Measurements of Deuteron Electro-Disintegration at Very High Recoil Momenta and Large 4-Momentum Transfers (Q^2)*, Ph.D. thesis, Florida International University, 11200 SW 8th St, Miami, FL 33199 (2020), <https://arxiv.org/abs/2009.11343>.